HOKKAIDO UNIVERSITY

Title	Origins of Al-rich chondrules: Clues from a compound Al-rich chondrule in the Dar al Gani 978 carbonaceous chondrite
Author(s)	Zhang, Ai-Cheng; Itoh, Shoichi; Sakamoto, Naoya et al.
Citation	Geochimica Et Cosmochimica Acta, 130, 78-92 https://doi.org/10.1016/j.gca.2013.12.026
Issue Date	2014-04-01
Doc URL	https://hdl.handle.net/2115/55712
Type	journal article
File Information	GCA_130_78-.pdf

Hokkaido University Collection of Scholarly and Academic Papers : HUSCAP

Origins of Al-rich chondrules: Clues from a compound Al-rich chondrule in the Dar al Gani 978 carbonaceous chondrite

Ai-Cheng Zhang [a,b,*], Shoichi Itoh [b,#], Naoya Sakamoto [c], Ru-Cheng Wang [a], and Hisayoshi Yurimoto [b,c]

[a] State Key Laboratory for Mineral Deposits Research, School of Earth Sciences and Engineering, Nanjing University, Nanjing 210046, China

[b] Department of Natural History Sciences, Hokkaido University, Sapporo 060-0810, Japan

[c] Isotope Imaging Laboratory, Creative Research Institution, Hokkaido University, Sapporo 001-0021, Japan

*Corresponding author. E-mail address: aczhang@nju.edu.cn

#Present address: Division of Earth and Planetary Sciences, Kyoto University, Kyoto 606-8502, Japan

Revised version to ***Geochimica et Cosmochimica acta***

ABSTRACT

Aluminum-rich chondrules are one of the most interesting components of primitive chondrites, because they have characteristics that are similar to both CAIs and ferromagnesian chondrules. However, their precursor and formation history remain poorly constrained, especially with respect to their oxygen isotopic distributions. In this study, we report on the petrography, mineralogy, oxygen isotope ratios, and rare-earth-element compositions of a sapphirine-bearing Al-rich chondrule (SARC) in the ungrouped chondrite Dar al Gani (DaG) 978. The SARC has a complex core-mantle-rim texture; while both the core and the mantle are mainly composed of Al-rich enstatite and anorthite with minor amounts of mesostasis, these regions are distinguished by the presence of Fe-rich spinel and sapphirine in the core and their absence in the mantle. The rim of the SARC consists mainly of Fe-rich olivine, enstatite, and Fe-Ni metal. Spinel and some olivine grains in the SARC are ^{16}O-rich, with Δ^{17}O values down to –20‰ and –23‰, respectively. Enstatite, sapphirine, and most olivine grains have similar Δ^{17}O values (~ –7‰), which are lower than those of anorthite and the mesostasis (including augite therein) (Δ^{17}O: ~ –3‰). Mesostasis from both the core and mantle have Group II rare-earth-element (REE) patterns; however, the core mesostasis has higher REE concentrations than the mantle mesostasis. These observations provide a strong indication that the SARC formed by the melting and crystallization of a mixture of materials from Group II Ca,Al-rich inclusions (CAIs) and ferromagnesian chondrules. Both spinel and olivine with ^{16}O-rich features could be of relict origin. The ^{16}O-poor isotopic compositions of most components in Al-rich chondrules can be explained by oxygen isotopic exchange between the melt and ^{16}O-poor nebular gas (Δ^{17}O: ~ –7‰) during melting in chondrule-forming regions; whereas the anorthite and mesostasis could have experienced further oxygen isotopic exchange with a relatively ^{16}O-poor reservoir (Δ^{17}O: ~ –3‰) on the parent body, likely during fluid-assisted thermal metamorphism. During the same thermal metamorphism event, spinel, olivine, some enstatite, and the mesostasis experienced Mg-Fe exchange to various extents.

INTRODUCTION

Aluminum-rich chondrules are defined as round objects in chondrites with igneous textures and high bulk Al_2O_3 contents (≥10 wt%; Bischoff and Keil, 1984). They have been observed in most groups of chondrites and have diverse textures and mineralogy (ordinary chondrites, Bischoff and Keil, 1984; Bischoff et al., 1989; Russell et al., 2000; Rubin, 2004; MacPherson and Huss, 2005; enstatite chondrites, Guan et al., 2006; carbonaceous chondrites, Sheng et al., 1991; Krot and Keil, 2002; Krot et al., 2002; Akaki et al., 2007; Zhang and Hsu, 2009). The bulk Al_2O_3 contents of Al-rich chondrules are intermediate between those of Ca,Al-rich inclusions (CAIs) and ferromagnesian chondrules (Russell et al., 2005). Because of this compositional feature, Al-rich chondrules can be used to assess possible genetic relationships between CAIs and ferromagnesian chondrules, which are the two main high-temperature crystallization products from the solar nebula preserved in chondritic meteorites.

Previous investigations have suggested that Al-rich chondrules could have formed by melting and crystallization of precursor mixtures composed of CAIs and ferromagnesian chondrules (Bischoff and Keil, 1984; Sheng et al., 1991; Krot and Keil, 2002; Krot et al., 2002; MacPherson and Huss, 2005; Zhang and Hsu, 2009), although Rubin (2004) proposed that amoeboid olivine aggregates (AOAs) could also be the precursor materials of some Al-rich chondrules. The key evidence for this conclusion includes high bulk Al_2O_3 contents, relict fragments of CAIs, and fractionated rare-earth-element (REE) patterns (e.g., Misawa and Nakamura, 1988; Sheng, 1992; Krot and Keil, 2002; Krot et al., 2006). In contrast, the oxygen isotopic compositions of most Al-rich chondrules in ordinary and enstatite chondrites ($\delta^{17,18}O$: ~ –15 to +5 ‰; Russell et al., 2000; Guan et al., 2006) are closely related to those of ferromagnesian chondrules (Krot et al., 2006). This led Russell et al. (2000) and Guan et al. (2006) to suggest that Al-rich chondrules were not significantly influenced by remelting of a hybrid mixture of ferromagnesian chondrules and ^{16}O-rich CAI materials, which have $\delta^{17,18}O$ values down to –70 ‰ (Gounelle et al., 2009). However, oxygen isotopic compositions of minerals are subject to resetting during thermal events (e.g., chondrule formation and parent body metamorphism). Therefore, without combining with other geochemical parameters, such as REE patterns, that can be diagnostic of CAIs, it is difficult to determine from these studies alone whether Al-rich chondrules have the same oxygen isotopic compositions as those of their precursors, or have experienced oxygen isotope exchange during melting of their precursors and/or after accretion onto the parent body.

The main purpose of this study is to constrain the precursor and formation history of Al-rich chondrules by studying the petrography, mineralogy, bulk composition, and *in situ* oxygen isotopes and REE compositions of a sapphirine-bearing Al-rich chondrule (abbreviated as SARC) with a core-mantle-rim texture from the Dar al Gani (DaG) 978, an ungrouped carbonaceous chondrite (Zhang and Yurimoto, 2013). The combination of REE with oxygen isotope ratios is used as indicators of CAI origin, and diffusion modeling of oxygen and Fe-Mg in minerals is used to constrain thermal history on the parent body. Preliminary results of this study were reported as conference abstracts (Zhang et al., 2011, 2013).

SAMPLE AND ANALYTICAL METHODS

Dar al Gani 978 is a type 3 ungrouped carbonaceous chondrite found in Libya (Choi et al., 2010; Zhang and Yurimoto, 2013). Zhang and Yurimoto (2013) reported detailed petrography and mineralogy of this ungrouped chondrite. Most grains of spinel and olivine in this chondrite are highly FeO-rich. Zhang and Yurimoto (2013) suggested that DaG 978 could have experienced parent-body thermal metamorphism temperature up to 850-950 K.

The petrography of the SARC from DaG 978 was studied using scanning electron microscopy (SEM; Hitachi 3400N II) at Nanjing University and field emission-SEM (FE-SEM; JEOL JSM-7000F) at Hokkaido University. Mineral chemistry of the SARC was determined by using electron probe micro-analysis (EPMA; JEOL 8100) at Nanjing University. The operating conditions employed for EPMA measurements were 15 kV accelerating voltage, 20 nA beam current, and a beam size of 1-2 μm. Natural and synthetic standards were used. The typical detection limits for oxides of most elements were better than 0.02 wt%. EPMA data were reduced using the ZAF correction procedure.

Bulk compositions of the core and mantle in the SARC and their respective mesostasis, were obtained using FE-SEM following the procedure of Zhang and Hsu (2009) under the analytical mode for irregularly outlined materials of the Point&ID Navigator in the X-ray spectroscopy (EDS; Oxford-INCA) system. The energy dispersive spectrometer scans a selected area and outputs the average results of elements in the selected area. Spinel and anorthite grains in sapphirine-bearing objects were used as standards for Si, Mg, Fe, Ca, Al, Cr, Na, and Ti with 100 s counting time; the compositions of these spinel and anorthite grains were previously measured by EPMA, and have confirmed homogeneous compositions among different grains.

Oxygen isotopic compositions of minerals in the SARC were measured using the Cameca IMS-1270 instrument at Hokkaido University. The primary ion beam was mass filtered positive Cs^+ ions of 20 keV and the beam spot size was ~ 3 μm in diameter. A primary beam current of ~ 20 pA was used to obtain a count rate of negative ^{16}O ions of ~ 1×10^7 cps. A normal-incident electron gun was utilized for charge compensation of the sputtered area. Negative ^{16}O ions were detected with an axial Faraday cup, while negative ^{17}O, ^{16}OH, and ^{18}O ions were detected with an axial electron multiplier, in magnetic peak jumping mode. A mass resolving power of ~ 5500 was used to separate ^{17}O from ^{16}OH. The instrumental mass fractionation effect was corrected using terrestrial spinel, anorthite, olivine, and augite standards (Yurimoto et al., 1994; Katayama et al., 2012; Kawasaki et al., 2012; Wakaki et al., 2013). The reported uncertainties of the individual analyses are expressed in 2σ, which were estimated by considering both the internal error of each measurement and the reproducibility of the standard measurements. After the measurements, all spots were evaluated using FE-SEM. Data from spots that overlapped undesirable minerals and/or cracks were rejected.

The REE concentrations of mesostasis in the SARC were determined with the Cameca IMS-6f instrument at Hokkaido University. The procedure was similar to that described in Yurimoto et al. (1989) and Wang and Yurimoto (1993). The primary beam was mass filtered $^{16}O^-$ of 14.5 keV and irradiated on the sample surface to a diameter of ~ 30 μm. Kinetic energy filtering was achieved by offsetting the sample acceleration voltage (−60 eV) while keeping the electrostatic analyzer voltage, as well as the width and position of the energy slit, constant. The energy bandwidth was 20 eV. The exit slit was set to a mass resolving power of ~ 500. Positive secondary ion intensities were counted, typically for 10 s, using the peak jumping mode. Each analysis included 20 cycles. Relative sensitivity factors between secondary ion intensity and concentration for each REE (relative to Si) were determined using the Takashima augite, for which REE contents have been well determined by instrumental neutron activation analysis (INAA) (Onuma et al., 1968).

RESULTS

Petrography and mineralogy of the SARC

The sapphirine-bearing Al-rich chondrule from DaG 978 has a round shape of approximately 1.5 mm in diameter. It has a complex core-mantle-rim texture (Fig. 1) based on the change of constituent minerals.

The core is approximately 700 μm in diameter and consists mainly of anhedral to euhedral enstatite and anorthite. The enstatite crystals contain thin and parallel cracks perpendicular to the elongate **c**-axis (Fig. 2a). These parallel cracks could have formed during the transformation from high-temperature protoenstatite into clinoenstatite (Yasuda et al., 1983). The most important characteristics of the core are the dense distribution of fine-grained spinel (<10 μm) and the presence of euhedral sapphirine in the mesostasis (Fig. 2a). The subhedral to euhedral spinel grains are enclosed not only by Al-rich enstatite and anorthite, but also by euhedral sapphirine (Fig. 2b). Sapphirine occurs mainly in the mesostasis (Fig. 2b). Besides sapphirine and spinel, the mesostasis in the core contains very fine-grained high-Ca pyroxene and anorthite (Fig. 2b). The spinel is FeO-rich, with Mg# values [=mol. % MgO/(MgO+FeO)] of 58-60 (Table 1). The anorthite has a composition of An_{87}-An_{89}. Most Al-rich enstatite grains in the core contain low Fs and Wo components ($En_{96.5\text{-}98.0}Fs_{0.6\text{-}2.1}Wo_{1.4}$) and have high Al_2O_3 contents (~11.0 wt%). The sapphirine has a composition close to its stoichiometry ($Mg_2Al_4SiO_{10}$) and contains low FeO (0.39-0.51 wt%). Its TiO_2 and Cr_2O_3 contents are 1.44-1.75 wt% and 1.09-1.42 wt%, respectively (Table 1). EDS results for the average compositions of the bulk core and its mesostasis are given in Table 2. Both the bulk core and its mesostasis have high average contents of Al_2O_3 (29.3 and 27.2 wt%, respectively) and FeO (5.4 and 4.6 wt%, respectively). The average Na_2O contents in the bulk core and its mesostasis are both 1.1 wt% (Table 2).

The mantle of the SARC is approximately 400 μm thick and is mainly composed of Al-rich enstatite, anorthite, and mesostasis (Fig. 3a). The core and the mantle are distinguished by the presence of spinel (core) and the lack of spinel (mantle) in the mineral assemblage (Fig. 3b). Unlike their counterparts in the core, Al-rich enstatite and anorthite in the mantle are coarser-grained (Fig. 3a), with some anorthite grains that are approximately 60 μm wide. Most Al-rich enstatite grains also contain thin and parallel cracks perpendicular to the **c** axis, whose formation could be related to the transformation from high-temperature protoenstatite into clinoenstatite. The mesostasis in the mantle consists mainly of relatively coarse-grained high-Ca pyroxene (up to 20 μm in diameter) and anorthite than those in the core mesostasis. Chemically zoned and Al-poor enstatite grains often occur in or adjacent to mesostasis in the mantle (Fig. 3c). It is noteworthy that some anhedral to subhedral olivine grains and FeNi metals (10-60 μm in size) occur locally in the mantle, close to the margin of this chondrule (Fig. 3d). Anorthite grains in the mantle contain slightly lower An components ($An_{82\text{-}87}$) than those in the core of the SARC (Table 1). Most coarse Al-rich enstatite grains ($En_{97.7\text{-}97.9}Fs_{0.6\text{-}}$

$_{0.8}Wo_{1.4-1.6}$) contain high Al_2O_3 (8.13-10.7 wt%) and low FeO (0.37-0.50 wt%) (Table 1). However, the zoned enstatite grains ($En_{77.4-97.6}Fs_{1.1-21.2}Wo_{0.8-1.7}$) in and adjacent to mesostasis contain lower Al_2O_3 (3.71-7.11 wt%) and higher FeO (0.73-14.0 wt%). The high-Ca pyroxene grains ($En_{31.6-48.5}Fs_{17.6-18.5}Wo_{34.0-50.7}$) in the mantle mesostasis are FeO-rich (Mg#=64.1-73.4) and have large variations in Al_2O_3 and TiO_2 contents (0.43-4.91 and 0.14-3.06 wt%, respectively). Olivine in the mantle is FeO-rich (Mg#=68.1-71.2). The average bulk compositions of the mantle and its mesostasis are also given in Table 2. Compared to the bulk core and its mesostasis, the bulk mantle and its mesostasis have higher average amounts of SiO_2 and CaO and lower average amounts of MgO and Al_2O_3 (Table 2). The bulk mantle and its mesostasis contain high FeO (4.5 and 6.6 wt%, respectively) and Na_2O (1.8 and 1.7 wt%, respectively).

The rim of the SARC is mainly composed of olivine, enstatite, and Fe-Ni-metal and occurs discontinuously (Figs. 1 and 4a). A few fine and irregular grains of anorthite are present in the rim; however, no apparent mesostasis was observed. At some sections, the olivine-enstatite assemblages are partially enclosed in the mantle (Fig. 4b). The texture and mineralogy of the rim, with round-shaped olivine and FeNi metal grains enclosed by enstatite, are almost the same as those of porphyritic olivine-pyroxene chondrules observed in DaG 978 (Zhang and Yurimoto, 2013). Olivine in the rim is also Fe-rich (Mg#=68.7-69.3) and is almost identical in composition to olivine in the mantle (Table 1). Enstatite grains ($En_{74.0-92.6}Fs_{6.5-24.3}Wo_{0.9-1.7}$) in the rim are usually low in Al_2O_3 (~ 1 wt%) and have a large variation in Mg# (75.3-93.4).

Oxygen isotopic compositions of the SARC

Minerals in the SARC have a large variation in oxygen isotopic composition (Table 3) and almost all data lie along the carbonaceous chondrite anhydrous minerals (CCAM) line (Fig. 5).

The oxygen isotopic compositions of more than ten spinel grains from the core of the SARC were measured. However, nine of the ten measurements, that show ^{16}O-enrichments to various degrees, were contaminated by surrounding minerals or cracks due to the small spinel grain sizes and were rejected. One spinel grain was successfully measured without contamination from surrounding minerals and cracks, and the result indicated ^{16}O-enrichment ($\Delta^{17}O$ = –19.9‰; Table 3). Sapphirine in the core mesostasis of the SARC has a small grain-to-grain variation in $\Delta^{17}O$ from –7.7 to –5.8‰ (Fig. 5; Table 3). The Al-rich enstatite grains in

the core of the SARC have oxygen isotopic compositions ($\Delta^{17}O$ = –7.5 to –3.7‰) similar to those of sapphirine. Anorthite from the core of the SARC is ^{16}O-poor (Table 3; Fig. 5) and has a small variation of oxygen isotopic compositions ($\Delta^{17}O$ = –4.6 to –2.7‰). The core mesostasis (not overlapping sapphirine) has oxygen isotopic compositions ($\Delta^{17}O$ = –4.2 to –1.0‰) similar to those of anorthite.

Aluminum-rich enstatite in the mantle of the SARC has oxygen isotopic compositions ($\Delta^{17}O$ = –8.8 to –3.8‰) similar to those in the core of the SARC. Oxygen isotopic compositions of anorthite ($\Delta^{17}O$ = –4.7 to 0.2‰) and mesostasis (including a 20-μm-size augite grain @95 therein shown in Fig. 3c) ($\Delta^{17}O$ = –3.3 to –0.6‰) in the mantle are also similar to those in the core of the SARC, respectively. Oxygen isotopic compositions of most olivine grains ($\Delta^{17}O$ = –8.8 to –3.8‰) in the mantle are similar to those of Al-rich enstatite (Table 3; Fig. 5); however, one analysis (@46, which is in the same olivine#1 grain with @49 and @51) shows a ^{16}O-rich oxygen isotopic composition with the $\Delta^{17}O$ value down to –11.6‰ (Table 3).

Enstatite in the rim of the SARC has oxygen isotopic compositions ($\Delta^{17}O$ = –8.2 to –6.6‰) generally similar to those in the core and the mantle. Differing from enstatite, olivine in the rim of the SARC has a large variation of oxygen isotopic composition among different grains, with $\Delta^{17}O$ varying from –23.0‰ to –4.5‰. Similar to those in olivine#1 grain, variable oxygen isotopic compositions within a few single olivine grains were observed (e.g., spots @132, @133, and @135 in olivine#3 grain; Table 3). However, based on the few measured spots of single olivine grains, it is difficult to determine whether there is gradual zoning of the oxygen isotopic compositions.

In summary, spinel and some olivine grains in the SARC are ^{16}O-rich, with $\Delta^{17}O$ down to –19.9‰ and –23.0‰, respectively. Al-rich enstatite, sapphirine, enstatite, and most olivine grains have oxygen isotopic compositions similar to each other ($\Delta^{17}O$: ~ –7‰). Meanwhile, anorthite and mesostasis (including the 20-μm-size augite therein) have similar oxygen isotopic compositions and are even more ^{16}O-poor ($\Delta^{17}O$: ~ –3‰) than those of Al-rich enstatite, sapphirine, enstatite, and most olivine grains.

Rare-earth-element compositions of mesostasis

Analytical results for REE in eight mesostasis samples from the core and the mantle of the SARC are given in Table 4 and the CI-normalized abundances of the REEs are plotted in

Fig. 6 (Anders and Grevesse, 1989). Both mesostasis in the core and mantle are enriched in REE and have Group II REE patterns with a flat light REE (LREE) pattern and a fractionated heavy REE (HREE) pattern (Fig. 6). However, the REE abundances of the core mesostasis (La ~ 102-157 × CI) are higher than those of the mantle mesostasis (La ~ 65-132 × CI; Fig. 6).

DISCUSSION

Precursor materials and melting environment of the Al-rich portion in the SARC

The precursor materials of an Al-rich chondrule are one of the key constraints to its origin. Previous investigations have suggested that some Al-rich chondrules are related to a mixture of CAIs and ferromagnesian chondrules, based on the bulk chemistry, the presence of relict fragments of CAIs, and fractionated REE patterns (e.g., Sheng, 1992; Russell et al., 2000; Krot and Keil, 2002; Krot et al., 2002; MacPherson and Huss, 2005; Zhang and Hsu, 2009). However, oxygen isotopic compositions ($\delta^{17,18}O$: ~ –15 to +5 ‰) of minerals in Al-rich chondrules from ordinary chondrites (Russell et al., 2000) and enstatite chondrites (Guan et al., 2006) are closely related to those of ferromagnesian chondrules. These results led them to suggest that the precursor materials of Al-rich chondrules are not simple mixtures of materials from CAIs and ferromagnesian chondrules (e.g., Russell et al., 2000; Guan et al., 2006). In this section, we will discuss our observations with respect to the possibility that the precursor materials of the Al-rich core and mantle in SARC are mixtures of materials from CAIs and ferromagnesian chondrules.

First, the Al-rich portion (including the core and the mantle) of the SARC has intermediate bulk chemistry and mineralogy between those of CAIs and ferromagnesian chondrules. On one hand, both the core and mantle of the SARC contain much higher Al_2O_3 (up to 29 wt%), relative to the amount in ferromagnesian chondrules. This is due to the dominance of Al-rich minerals (spinel, anorthite, and Al-rich pyroxene) in the core and mantle of the SARC. On the other hand, the core and mantle have lower CaO contents than typical CAIs, which are due to the presence of low-Ca pyroxene, rather than high-Ca pyroxene in SARC core and mantle. Olivine and FeNi-metal, the common minerals of ferromagnesian chondrules, are also present in the mantle. Thus, the petrography, bulk compositions, and mineralogy support that the precursor material of the Al-rich portion (core and mantle) of the SARC is a mixture of materials from CAIs and ferromagnesian chondrules.

Second, mesostasis from both the core and mantle of the SARC have REE patterns similar to those of Group II refractory inclusions. The Group II REE pattern is usually explained by fractional removal of some ultra-refractory elements, which could have concentrated in early condensed solids from a nebula (Boynton, 1975; Davis and Grossman, 1979; Palme et al., 1982). This REE pattern is only consistent with an origin of refractory inclusions, although it does not occur in all refractory inclusions. Thus, although the REE patterns of the bulk Al-rich portion in the SARC could be slightly different from those of mesostasis, due to the igneous fractionation of pyroxene and anorthite, REE pattern should still be similar to that of Group II refractory inclusions because REEs are incompatible in anorthite and enstatite; therefore REEs should be concentrated in mesostasis. The Al-rich portion of the SARC contains very minor amounts of olivine, so that it seems unlikely that amoeboid olivine aggregate (AOA) precursor material is a main contributor to the precursor materials of the Al-rich portion in SARC. Thus, the REE patterns of mesostasis from the core and mantle strongly suggest that the precursor materials of the Al-rich portion in the SARC are related to materials from Group II CAIs.

Third, it is well accepted that primitive refractory inclusions are ^{16}O-rich, whereas chondrules are usually ^{16}O-poor (Yurimoto et al., 2008). Of course, in the literature (e.g., Maruyama et al., 1999; Yurimoto and Wasson, 2002; Maruyama and Yurimoto, 2003; Jones et al., 2004; Nagashima et al., 2012), there are a few reports that some minerals in chondrules also have ^{16}O-rich oxygen isotopic compositions. However, most of these investigators suggested that the ^{16}O-rich features could be related to relict materials from Ca,Al-rich inclusions or amoeboid olivine aggregates. Alternatively, Jones et al. (2004) also proposed that the earliest nebular solids from which chondrules formed are ^{16}O-rich as discussed by Kobayashi et al. (2003), since no petrographic and mineralogical supporting a relict origin from refractory inclusions was observed in their study. In this study, we favor that the ^{16}O-rich feature of the spinel in the SARC is additional evidence that supports the precursor material of the core in the SARC is related to materials from CAIs.

Thus, it is concluded that the precursor of the Al-rich portion in the SARC must have been a mixture of materials from CAIs with a Group II REE pattern and ferromagnesian chondrules. The materials from CAIs should be dominant in the mixture. We can also infer that the minerals (e.g., Al-rich enstatite and sapphirine) crystallized from in the Al-rich portion of the SARC were more ^{16}O-rich than those of the minerals crystallized from ferromagnesian chondrules (e.g., enstatite and most olivine grains in the rim of the SARC)

and those of the ferromagnesian chondrule components in most chondrites (e.g., Krot et al., 2006; Yurimoto et al., 2008; Ushikubo et al., 2012; Tenner et al., 2013). Instead, in contrast to this inference, the oxygen isotope compositions of Al-rich enstatite and sapphirine in the SARC are similar to those of enstatite and most olivine grains in the rim. This observation is similar to those from previous investigations (Russell et al., 2000; Guan et al., 2006). It is very likely that the oxygen isotopic compositions of most minerals in the Al-rich portion of the SARC had been reset during melting of the Al-rich portion of the SARC precursor materials and/or after accretion into the parent body. In this study, we suggest that the oxygen isotopic compositions of most minerals crystallized from the Al-rich portion of the SARC (except the ^{16}O-rich spinel) had been reset during the heating and melting event of their precursor materials in the nebula; whereas the oxygen isotopic compositions of anorthite and mesostasis were further modified on the parent body. In addition, the ferromagnesian components (including the rim and olivine and metal in the mantle) in the SARC could have formed in a separate process (will be discussed in detail later on), which is not related to the precursor materials of the Al-rich portion of the SARC and their melting.

Yu et al. (1995) performed high-temperature oxygen isotopic exchange experiments, which indicated that oxygen isotopic compositions between a chondrule analogue melt and water vapor could reach equilibrium on a scale of minutes. Therefore, if the precursor materials of the Al-rich portion in the SARC were melted, the melt could readily approach oxygen isotopic equilibrium with the surrounding ^{16}O-poor nebular gas. Meanwhile, the ^{16}O-rich spinel could be of relict origin during melting of the precursor. The self-diffusion speed of oxygen in solid spinel is very slow (Ryerson and McKeegan, 1994). At 1400 K, an oxygen diffusion length of 1 μm in spinel could require ~ 170 years, which is much longer than the duration of high temperature in chondrule-forming events (probably tens of hours, Desch et al. 2012). Thus, it is reasonable that relict spinel can retain its ^{16}O-rich feature during the chondrule-forming event, while minerals crystallized from the melt adopt ^{16}O-poor features (Δ^{17}O: ~ −7‰) due to melt-gas oxygen isotopic exchange in the nebula. The similarity between oxygen isotopic compositions of Al-rich enstatite and sapphirine in the SARC and those of ferromagnesian chondrule materials from other chondrites (e.g., Krot et al., 2006; Yurimoto et al., 2008; Ushikubo et al., 2012; Tenner et al., 2013) also supports this inference.

Crystallization of the Al-rich core and mantle in the SARC

The ferromagnesian rim in SARC has a distinctly different texture and mineral assemblages, relative to those of the Al-rich portion in the SARC. Ferromagnesian

components in the rim, as well as Fe-rich olivine in the mantle, were probably attached onto the mantle of SARC during solidification of the mantle. Their formation will be discussed separately in the following section. In this section, we focus mainly on the crystallization of the Al-rich portion in the SARC. The boundary between the core and mantle of the SARC implies three possible interpretations for the core-mantle texture of the Al-rich portion: 1) The core and mantle may have formed during two heating/melting events in the nebula (e.g., Akaki et al., 2007). 2) The core and mantle formed under a single heating/melting event in the nebula and crystallization proceeded from the mantle to the core. 3) The core and mantle formed under a single heating/melting event in the nebula and crystallization proceeded from the core to the mantle.

Akaki et al. (2007) studied a compound Al-rich chondrule from Allende, which also contains distinct textural domains. They proposed a model of two heating/melting events to interpret the texture and oxygen isotopic distribution of olivine in that Al-rich chondrule. In the model, the core, which is considered as the primary chondrule, was formed during the first heating/melting event, and the mantle was then formed by the melting of core plagioclase and a porous dust clump that surrounded the primary chondrule. For the case of the SARC, this model can explain the decrease in the REE concentrations of mesostasis from the core to the mantle, assuming that the dust clump is REE-poor. However, this model may have difficulty in explaining the presence of sapphirine in the core. Crystallization experiments conducted by Sheng (1992) suggested that sapphirine is a metastable phase in Al-rich chondrules. Thus, if the core was reheated to ~ 1260 °C, sapphirine would likely have disappeared from the phase assemblage. In this study, we observed that most Al-rich enstatite grains in the core and mantle of the SARC are clinoenstatite that transformed from high-temperature protoenstatite, based on their parallel cracks perpendicular to the **c** axis (Yasuda et al., 1983). This indicates that, at a minimum, both the core and mantle crystallized above 1000 °C (Yasuda et al., 1983). If the temperature were significantly higher, sapphirine would have disappeared during a second heating/melting event, which is clearly inconsistent with its presence in the core. Thus, it is unlikely that the core and mantle of the SARC were formed by two separate heating/melting events.

The model that the core and mantle of the SARC formed under a single heating/melting event is supported by the similarity of REE patterns of the core and mantle mesostasis, especially one of the REE analyses of the mantle mesostasis overlaps with those of the core mesostasis. Meanwhile, the variation of REE concentrations in the mesostasis would also be

a powerful indicator of the crystallization sequence. Anorthite and enstatite are the major components in the Al-rich portion of the SARC and are incompatible for REEs; therefore, the REE concentrations of the melt should tend to increase with the fractionation of anorthite and enstatite during crystallization. Also fractionation of primary anorthite during crystallization would cause deeper negative Eu anomaly of core mesostasis vs. mantle mesostasis. Therefore, the variation of REE concentrations of the mesostasis supports that the crystallization proceeded from the mantle to the core (e.g., Fig. 6). This conclusion is also consistent with the euhedral shape and large grain sizes of most anorthite and enstatite in the mantle; whereas the anhedral to euhedral shape and small grains of anorthite and enstatite in the core could be due to space limitations during crystallization. The slightly lower An value of anorthite in the mantle could be due to a higher degree of secondary sodium-metasomatism in the mantle, relative to that in the core. The slightly higher Na_2O content in mesostasis of the mantle, relative to that of the core also supports this interpretation. However, this crystallization sequence (from the mantle to the core) seems to conflict with the presence of relict spinel, because relict spinel grains are the preferred nucleation sites if there is no significant temperature gradient between the core and the mantle.

If the crystallization of the Al-rich portion started from the core by nucleation on relict spinel, then the variation of the anorthite An values from the core to the mantle is consistent with the crystallization sequence, meaning that no secondary sodium-metasomatism was required. However, to explain the relatively low REE concentrations of the mantle mesostasis, when compared to those from the core, would require the addition of REE-poor material during crystallization of the mantle. The olivine and FeNi-metal could represent this REE-poor material; however, the minor amount of olivine and FeNi-metal observed in the mantle of the SARC does not seem sufficient to explain the dilution effect of REE in the mantle.

Based on the discussion above, melting under a single heating/melting event and crystallization that proceeded from the mantle to the core seems to be the most likely scenario for the formation and crystallization of the Al-rich portion in the SARC. This single stage heating event model is also consistent with the almost same oxygen isotopic compositions of Al-rich enstatite from the core and the mantle; chondrules formed during heating events at different local regions may preserve various primary oxygen isotopic compositions (Ushikubo et al., 2012). The different bulk composition and mineralogy in mesostasis from the core and mantle could be due to the formation separate melt pockets during crystallization of enstatite and anorthite.

Tronche et al. (2007) have performed experiments to understand the effects of bulk compositions, peak temperatures, and cooling rates on the mineralogy and texture of Al-rich chondrules. They concluded that the textures of anorthite-rich compositions are more sensitive to peak temperatures than they are to cooling rates. In their run products, higher peak temperatures response to coarser textures; meanwhile, at the same peak temperatures, slower cooling rates lead to lower aspect ratios of anorthite laths. For the case of the Al-rich portion of the SARC, which is anorthite-rich (Fig. 1), the sizes of anorthite laths in the mantle are comparable to those of run products cooled from a peak temperature of 1475 °C (Tronche et al., 2007) and are much coarser than those of experiments cooled from a peak temperature of 1401 °C and 1452 °C (Tronche et al., 2007). And, the aspect ratios of anorthite grains are comparable to those of run products cooled at 5-10 °C/h. This indicates that the mantle of the SARC could have crystallized from a peak temperature between 1452-1475 °C and at cooling rates of 5-10 °C/h. In addition, as pointed out by Sheng (1992), sapphirine is a metastable phase during crystallization and not stable at 1253-1260 °C. Therefore, the presence of sapphirine in the core mesostasis implies that the core could have completed its crystallization below 1253 °C. This inference is consistent with the various textures of run products cooled from different peak temperatures (Tronche et al., 2007).

Formation of ferromagnesian components in the SARC

The ferromagnesian components in the SARC include the chondrule-like rim, and olivine and FeNi metal grains observed in the mantle. The olivine grains in the mantle have similar petrographic, mineralogical, and oxygen isotopic features to those in the rim, which suggests that the ferromagnesian components in the mantle and the rim have a common origin.

All olivine grains in the SARC have sub-rounded to rounded shapes and all olivine grains in the rim are embedded in enstatite. This feature is similar to that of most porphyritic olivine-pyroxene chondrules (Zhang and Yurimoto, 2013), which implies similar formation processes. Most olivine grains have ^{16}O-poor oxygen isotopic compositions similar to that of enstatite, which is also a typical feature of porphyritic olivine-pyroxene chondrules from unmetamophosed carbonaceous chondrites (Ushikubo et al. 2012; Tenner et al., 2013). Therefore, the oxygen isotopic compositions of enstatite may represent those of the chondrule-forming region. Interestingly, a few olivine grains are ^{16}O-rich to various degrees. Similar ^{16}O-rich isotopic compositions in chondrule olivine have also been previously reported (e.g., Hiyagon and Hashimoto, 1999; Jones et al., 2004; Nagashima et al., 2012;

Ushikubo et al., 2012; Tenner et al., 2013) and are likely of relict origin, although Jones et al. (2004) also proposed an alternative interpretation that the earliest nebular solids from which chondrules formed had $\delta^{17}O$ and $\delta^{18}O$ values around −50‰. The relict origin for these olivine grains could be similar to the origin of the ^{16}O-rich spinel discussed earlier or of the ^{16}O-rich olivine of a ^{16}O-rich chondrule (Kobayashi et al., 2003), as both phases have similarly slow oxygen diffusion rates under chondrule-forming conditions (Ryerson et al., 1989; Ryerson and McKeegan, 1994). The ^{16}O-rich olivine in the SARC could also be of relict origin due to incomplete melting during the chondrule-forming event (not the event that caused melting of the precursor of the Al-rich portion in SARC). Analyses that indicate intermediate $\Delta^{17}O$ probably reflect various contributions from ^{16}O-rich (e.g., $\Delta^{17}O$= –23‰) and ^{16}O-poor (e.g., $\Delta^{17}O$= –7‰) domains within each measurement spot. However, one olivine grain in the SARC has an extremely low $\Delta^{17}O$ (–23‰) that is almost identical to that of olivine in pristine CAIs and AOAs (Hiyagon and Hashimoto, 1999; Komatsu et al., 2001; Yurimoto and Wasson, 2002; Imai and Yurimoto, 2003; Itoh et al., 2004; Itoh et al., 2007). In addition, olivine grains from DaG 978 AOA have similar CaO contents (<0.1 wt%) to those in the SARC (Zhang and Yurimoto, 2013), and both are lower in CaO contents than olivine from CAIs (CaO >0.1 wt%) in the same sample (Zhang and Yurimoto, 2013). This indicates that the ^{16}O-rich feature of some olivine grains in the SARC could have been derived from AOAs.

Post-crystallization processes in the SARC

One post-crystallization process recorded in SARC involves iron-enrichment in the oxide and silicate minerals. For example, enstatite along cracks and grain boundaries is FeO-enriched, which indicates that Fe-Mg interdiffusion occurred after the crystallization of enstatite. This interpretation is supported by the fact that sapphirine and most enstatite (Al-rich and Al-poor) grains in the SARC are FeO-poor, with Mg# values up to 99, suggesting that they initially formed in a FeO-depleted system. Spinel and olivine are also FeO-rich (Mg#: ~ 60 and 70, respectively) and are highly unequilibrated with FeO-poor enstatite. The Mg# values of spinel and olivine are instead similar to those of other grains of spinel and olivine from DaG 978 (Zhang and Yurimoto, 2013). Therefore, the FeO-rich features of spinel and olivine indicate secondary processes involving Mg-Fe exchange in the oxides and silicates, probably due to thermal metamorphism on the parent body. Zhang and Yurimoto (2013) suggested that the metamorphic temperature on the parent body of DaG 978 could be up to 850-950 K, based on spinel-olivine geothermometic calculations.

The other post-crystallization process recorded in the SARC involves the exchange of oxygen isotopes in anorthite and mesostasis (including a relatively coarse mesostasis augite grain up to 20 μm in size). The Al-rich portion in the SARC has an igneous texture; therefore, its components, except for relict spinel, should have nearly identical $\Delta^{17}O$ (c.f., Ushikubo et al., 2012). However, the present data indicate that anorthite and mesostasis (very fine-grained augite and anorthite/glass therein) have higher $\delta^{18}O$ and $\Delta^{17}O$ than enstatite, olivine, and sapphirine. This oxygen isotopic difference cannot be explained by melt-gas oxygen isotopic exchange during crystallization of the SARC, because the oxygen isotopic distribution in different minerals is not correlated with their crystallization sequence. For instance, sapphirine in mesostasis and enstatite have similar $\Delta^{17}O$ values that are lower than those of anorthite and mesostasis. Oxygen usually has faster diffusion rates in anorthite and mesostasis when compared to in pyroxene, olivine, and spinel (Ryerson et al., 1989; Ryerson and McKeegan, 1994); therefore, it is likely that the high $\Delta^{17}O$ of anorthite and mesostasis in the SARC is due to secondary oxygen isotope exchange after the solidification of the SARC (e.g., Wasson et al., 2001; Krot et al., 2008; Rudraswami et al., 2011). In addition, it is also possible that oxygen isotopic exchange in both anorthite and mesostasis, as well as the Mg-Fe exchange in minerals in the SARC, occurred during the same thermal metamorphic event on the parent body.

To further evaluate the feasibility of and conditions for O-isotope and Fe-Mg exchange on the parent body of DaG 978, the diffusion of oxygen and Fe-Mg in different minerals under anhydrous and hydrous conditions was calculated based on elemental diffusion coefficients for different minerals available in the literature and with various assumptions (Giletti et al., 1978; Freer and O'Reilly, 1980; Hallwig et al., 1982; Jaoul et al., 1983; Elphick et al., 1988; Farver, 1989; Ryerson et al., 1989; Ryerson and McKeegan, 1994; Hier-Majumder et al. 2005; Chakraborty, 2010). The minimum temperatures and durations (solid curves in Fig. 7) are constrained according to the estimated oxygen and Fe-Mg diffusion lengths in various minerals (30 and 10 μm for oxygen diffusion in anorthite and augite, respectively; 5, 15, 10, and 5 μm for Fe-Mg interdiffusion in spinel, olivine, augite, and in Al-poor enstatite, respectively).

The required diffusion temperatures and durations (dashed curves in Fig. 7) were also calculated for 1 μm diffusion of oxygen in spinel and olivine. These diffusion temperatures and durations likely represent upper limits because no oxygen isotopic compositions of spinel

and olivine were observed to be similar to those of anorthite and mesostasis, even if spinel and olivine were measured near the grain boundaries.

Diffusion calculations under anhydrous conditions (Fig. 7a) have two major implications. First, for a given temperature and time duration, the diffusion distance of oxygen in anorthite is approximately twice the distance of Fe-Mg interdiffusion in forsterite. This suggests that the oxygen isotopic composition of anorthite was changed when the Mg-Fe content of olivine was re-equilibrated during metamorphism on the parent body. However, it is difficult to explain the ^{16}O-poor composition of augite in the mesostasis by oxygen diffusion during the metamorphic event because the required temperature and duration for oxygen diffusion in augite is above those for oxygen diffusion in spinel and olivine (Fig. 7a). One possibility is that the augite is a metamorphic crystal crystallized during the metamorphic event (e.g. Rudraswami et al., 2011).

Second, in order to achieve equilibrium of the oxygen isotopic composition in anorthite, as well as the Fe-Mg compositions in spinel, forsterite, and for Fe to penetrate into Al-poor enstatite by diffusion, the estimated diffusion duration is around 1 Myr at a temperature of 850-950 K, which seems to be likely for a chondrite with a petrologic type of 3.6 (Zhang and Yurimoto, 2013). Therefore, if the large augite grain with high Δ^{17}O (−3‰) in the mesostasis crystallized during thermal metamorphism on the parent body, then it is likely that the oxygen isotopic exchange in anorthite and the Fe-Mg diffusion in spinel, olivine, and enstatite occurred under anhydrous metamorphic conditions.

All the diffusion curves measured under aqueous fluid saturated conditions (Fig. 7b) have significant shifts to lower temperatures at a given time duration, when compared with those measured under anhydrous conditions. This indicates that the Mg-Fe and oxygen isotopic exchange in minerals of the chondrule could have occurred easily under some degree of hydrous conditions because the presence of aqueous fluid significantly enhances the diffusion rates of oxygen and Fe-Mg in minerals. However, it should be noted that the diffusion coefficients under water saturated conditions used in Fig. 7 may be too large to constrain the O isotopic exchange of ^{16}O-rich minerals and that the experimental diffusion coefficients have high uncertainties compared with those under anhydrous conditions. Considering the presence of low-temperature alteration products (e.g., secondary nepheline) in DaG 978 (Zhang and Yurimoto, 2013), it is possible that the presence of water during thermal metamorphism under hydrous conditions assisted elemental and isotopic exchange in minerals.

Model for the formation of the SARC and comparison with other Al-rich chondrules

These discussions indicate that the SARC in DaG 978 has experienced multiple formation processes, which involved the mixing and melting of materials from refractory inclusions and ferromagnesian chondrules. The most probable model for the formation of the SARC includes the following stages (Fig. 8). a) Condensation of a CAI from ^{16}O-rich nebular gas ($\Delta^{17}O < -20‰$) where ultra-refractory components have been removed. This process resulted in the Group II REE pattern of the CAI. b) The Group II CAI was then transported into the chondrule-forming region, where it mixed with ferromagnesian material (that forms chondrule and/or matrix of chondrites). c) The hybrid between the Group II CAI and ferromagnesian material was melted, probably by a heating event related to chondrule-forming events, and experienced oxygen isotope exchange in a ^{16}O-poor chondrule-forming region ($\Delta^{17}O = -7‰$). Based on the texture comparison between SARC and those of experimental run products by Tronche et al. (2007), the peak crystallization temperature of the Al-rich portion of SARC was likely between 1452-1475 °C. However, in this heating event, spinel grains were not melted and retained their original ^{16}O-rich oxygen isotopic compositions. d) Upon cooling, the Al-rich melt crystallized from the mantle to the core. Some ferromagnesian chondrule materials were attached on the Al-rich melt and some fragments are partly or totally encapsulated in the Al-rich melt. e) After accretion into the parent body of DaG 978, anorthite and mesostasis in the SARC experienced oxygen isotopic exchange with relatively ^{16}O-poor fluid ($\Delta^{17}O$: –3‰) during fluid-assisted thermal metamorphism; during this process, spinel, olivine, some enstatite, and mesostasis experienced Mg-Fe exchange.

Interestingly, two other sapphirine-bearing Al-rich chondrules (USNM 3510 and BG82CLII) and a few previously reported cordierite-bearing Al-rich chondrules (Fuchs, 1969; Sheng et al., 1991; Akaki et al., 2007) also have similarly complex textures and mineral assemblages. All of these sapphirine and cordierite-bearing Al-rich chondrules have complex core-mantle features and their dominant Al-rich minerals are anorthite and Al-rich enstatite, rather than Al-rich diopside. In addition, small spinel grains are typically enclosed by anorthite, Al-rich enstatite, sapphirine or cordierite. The main difference among these complex Al-rich chondrules is the variation in the abundance of primary olivine from these Al-rich melts. The similarity in petrographic texture, mineral assemblage, and even oxygen isotopic composition among these sapphirine-bearing and cordierite-bearing Al-rich chondrules may indicate that they have experienced similar formation processes. The

differences in mineralogy between these Al-rich chondrules could be due to variety in the bulk compositions of their precursor materials. Compared to the Al-rich chondrules with complex textures, Al-rich chondrules with simple textures could have experienced high enough temperatures that would have melted all precursor materials, which would have allowed for near-complete oxygen isotope exchange with surrounding nebular gas in chondrule-forming regions. If correct, it could well explain the similarity in the oxygen isotopic compositions of most Al-rich chondrules when compared to those of ferromagnesian chondrules. However, although our oxygen isotope and REE data show that Al-rich chondrules could have formed by melting of hybrid of materials from CAIs and chondrules, some Al-rich chondrules contain no diagnostic evidence for the existence of CAI precursors. For example, MacPherson and Huss (2005) measured trace-element compositions for eleven Al-rich chondrules from unequilibrated ordinary chondrites. And no Group II REE patterns were observed for these 11 Al-rich chondrules. Thus, it suggests that some of these Al-rich chondrules, if not all, cannot be explained by the hybrid model inferred from this study.

CONCLUSIONS

A sapphirine-bearing Al-rich chondrule (SARC) was observed in the DaG 978 ungrouped type 3 carbonaceous chondrite. Petrographic, mineralogical, and SIMS oxygen isotope and REE geochemical analyses were conducted and the following conclusions were drawn:

1) The ^{16}O-rich spinel and olivine in the SARC are of relict origin.
2) The high bulk Al_2O_3 contents, the presence of relict spinel, and the characteristic Group II REE composition in mesostasis strongly indicate that the precursor of the Al-rich portion of the SARC is a mixture of materials from CAIs and ferromagnesian chondrules.
3) The Al-rich portion of the SARC experienced melt-gas oxygen isotope exchange in the chondrule-forming region, which could well explain why the oxygen isotopic compositions of most Al-rich chondrules are similar to those of ferromagnesian chondrules.
4) The presence of ^{16}O-rich olivine indicates that AOAs contributed in some manner to the formation of ferromagnesian chondrules.

5) After accretion onto the parent body of DaG 978, components in the SARC experienced oxygen and Fe-Mg exchange to various degrees, likely during fluid-assisted thermal metamorphism.

ACKNOWLEDGEMENTS

We thank Dr. Shogo Tachibana for constructive discussion. We are grateful to the critical and helpful comments by Dr. Yunbin Guan, Dr. Travis Tenner, an anonymous reviewer, and Associate Editor Prof. Sara Russell. This study is supported by a Monkasho grant to H. Yurimoto, research grants (Nos. 41073052 and 41373065) from the National Science Foundation of China (NSFC) and a Fellowship Grant-in-Aid from the Japan Society for the Promotion of Science (JSPS) to A.C. Zhang.

REFERENCES

Akaki T., Nakamura T., Noguchi T. and Tsuchiyama A. (2007) Multiple formation of chondrules in the early solar system: Chronology of a compound Al-rich chondrule. *The Astrophysical Journal* **656**, L29–L32.

Anders E. and Grevesse N. (1989) Abundances of the elements-Meteoritic and solar. *Geochimica et Cosmochimica Acta* **53**, 197–214.

Bischoff A. and Keil K. (1984) Al-rich objects in ordinary chondrites: Related origin of carbonaceous and ordinary chondrites and their constituents. *Geochimica et Cosmochimica Acta* **48**, 693–709.

Bischoff A., Palme H. and Spettel B. (1989) Al-rich chondrules from the Ybbsitz H4-chondrite: evidence for formation by collision and splashing. *Earth and Planetary Science Letters* **93**, 170–180.

Boynton W. V. (1975) Fractionation in the solar nebula: condensation of yttrium and the rare earth elements. *Geochimica et Cosmochimica Acta* **39**, 569–584.

Chakraborty S. (2010) Diffusion coefficients in olivine, wadsleyite and ringwoodite. *Reviews in Mineralogy & Geochemistry* **72**, 603–639.

Davis A. M. and Grossman L. (1979) Condensation and fractionation of rare earths in the solar nebula. *Geochimica et Cosmochimica Acta* **43**, 1611–1632.

623 Desch S. J., Morris M. A., Connolly H. C. Jr. and Boss A. P. (2012) The importance of
624 experiments: Constrains on chondrule formation models. *Meteoritics & Planetary*
625 *Science* **47**, 1139–1156.

626 Dimanov A. and Wiedenbeck M. (2006) (Fe,Mn)-Mg interdiffusion in natural diopside: effect
627 of pO_2. *European Journal of Mineralogy* **18**, 705–718.

628 Elphick S. C., Graham C. M. and Dennis P. F. (1988) An ion microprobe study of anhydrous
629 oxygen diffusion in anorthite: A comparison with hydrothermal data and some
630 geological implications. *Contrib Mineral Petrol* **100**, 490–495.

631 Farver J. (1989) Oxygen diffusion in diopside with application to cooling rate determinations.
632 *Earth and Planetary Science Letters* **92**, 386–396.

633 Freer R. and O'Reilly W. (1980) The diffusion of Fe^{2+} ions in spinels with relevance to the
634 process of maghemitization. *Mineralogical Magazine* **43**, 889–899.

635 Fuchs L. H. (1969) Occurrence of cordierite and aluminous orthoenstatite in the allende
636 meteorite. *The American Mineralogist* **54**, 1645–1653.

637 Ganguly J. and Tazzoli V. (1994) Fe^{2+}-Mg interdiffusion in orthopyroxene: Retrieval from the
638 data on intracrystalline exchange reaction. *American Mineralogist* **79**, 930–937.

639 Giletti B. J., Semet M. P. and Yund R. A. (1978) Studies in diffusion-III. Oxygen in feldspars:
640 An ion microprobe determination. *Geochimica et Cosmochimica Acta* **42**, 45–57.

641 Gounelle M., Krot A. N., Nagashima K. and Kearsley A. (2009) Extreme ^{16}O enrichment in
642 calcium-aluminum-rich inclusions from the Isheyevo (CH/CB) chondrite. *The*
643 *Astrophysical Journal* **698**, L18–L22.

644 Guan Y. B., Huss G. R., Leshin L. A., MacPherson G. J. and McKeegan K. D. (2006) Oxygen
645 isotope and ^{26}Al-^{26}Mg systematics of aluminum-rich chondrules from unequilibrated
646 enstatite chondrites. *Meteoritics & Planetary Science* **41**, 33–47.

647 Hallwig D., Schachtner R. and Sockel H. G. (1982) Diffusion of magnesium, silicon and
648 oxygen in Mg_2SiO_4 and formation of the compound in the solid state. *In*: Reactivity in
649 Solids. Dyrek K., Habor J., and Nowotry J. (eds) *Proc Intl Symp* (9th). pp166–169.

650 Hier-Majumder S., Anderson I. M. and Kohlstedt D. L. (2005) Influence of protons on Fe-Mg
651 interdiffusion in olivine. *Journal of Geophysical Research* 110:B02202,
652 doi:10.1029/2004JB003292.

Hiyagon H. and Hashimoto A. (1999) ^{16}O excesses in olivine inclusions in Yamato-86009 and Murchison chondrules and their relation to CAIs. *Science* **283**, 828–831.

Imai H. and Yurimoto H. (2003) Oxygen isotopic distribution in an amoeboid olivine aggregate from the Allende CV chondrite: Primary and secondary processes. *Geochimica et Cosmochimica Acta* **67**, 765–772.

Itoh S., Kojima H. and Yurimoto H. (2004) Petrography and oxygen isotopic compositions in refractory inclusions from CO chondrites. *Geochimica et Cosmochimica Acta* **68**, 183–194.

Itoh S., Russell S. S. and Yurimoto H. (2007) Oxygen and magnesium isotopic compositions of amoeboid olivine aggregates from the Semarkona LL3.0 chondrite. *Meteoritics & Planetary science* **42**, 1241–1247.

Jaoul O., Houlier B., and Abel F. (1983) Study of ^{18}O diffusion in magnesium orthosilicate by nuclear microanalysis. *Journal of Geophysical Research* **88**, 613–624.

Jones R. H., Leshin L. A., Guan Y., Sharp Z. D., Durakiewicz T. and Schilk A. J. 2004. Oxygen isotope heterogeneity in chondrules from the Mokoia CV3 carbonaceous chondrite. *Geochimica et Cosmochimica Acta* 68, 3423–3438.

Katayama J., Itoh S. and Yurimoto H. (2012) Oxygen isotopic zoning of reversely zoned melilite crystals in a fluffy type A Ca-Al-rich inclusions from the Vigarano meteorite. *Meteorit. Planet. Sci.* **47,** 2094–2106.

Kawasaki N., Sakamoto N. and Yurimoto H. (2012) Oxygen isotopic and chemical zoning of melilite crystals in a type A Ca-Al-rich inclusion of Efremovka CV3 chondrite. *Meteorit. Planet. Sci.* **47,** 2084–2093.

Kobayashi S., Imai H. and Yurimoto H. (2003) New extreme ^{16}O-rich reservoir in the early solar system. *Geochem. J.* **37,** 663-669.

Kohn M. J. (1999) Why most “dry” rocks should cool “wet”. *American Mineralogist* **84**, 570–580.

Komatsu M., Krot A. N., Petaev M. I., Ulyanov A. A., Keil K. and Miyamoto M. (2001) Mineralogy and petrography of amoeboid olivine aggregates from the reduced CV3 chondrites Efremovka, Leoville and Vigarano: Products of nebular condensation, accretion and annealing. *Meteoritics & Planetary Science* **36**, 629–641.

683 Krot A. N. and Keil K. (2002) Anorthite-rich chondrules in CR and CH carbonaceous
684 chondrites: Genetic link between calcium-aluminum-rich inclusions and ferromagnesian
685 chondrules. *Meteoritics & Planetary Science* **37**, 91–111.

686 Krot A. N., Hutcheon I. D. and Keil K. (2002) Plagioclase-rich chondrules in the reduced CV
687 chondrites: Evidence for complex formation history and genetic links between calcium-
688 aluminum-rich inclusions and ferromagnesian chondrules. *Meteoritics & Planetary*
689 *Science* **37**, 155–182.

690 Krot A. N., Yurimoto H., McKeegan K. D., Leshin L., Chaussidon M., Libourel G., Yoshitake
691 M., Huss G. R., Guan Y. and Zanda B. (2006) Oxygen isotopic compositions of
692 chondrules: Implications for evolution of oxygen isotopic reservoirs in the inner solar
693 nebula. *Chemie der Erde* **66**, 249–276.

694 Krot A. N., Chaussidon M., Yurimoto H., Sakamoto N., Nagashima K., Hutcheon I. D. and
695 MacPherson G. J. (2008) Oxygen isotopic compositions of Allende Type C CAIs:
696 Evidence for isotopic exchange during nebular melting and asteroidal metamorphism.
697 *Geochimica et Cosmochimica Acta* **72**, 2534–2555.

698 MacPherson G. J. and Huss G. R. (2005) Petrogenesis of Al-rich chondrules: Evidence from
699 bulk compositions and phase equilibria. *Geochimica et Cosmochimica Acta* **69**, 3099–
700 3127.

701 Maruyama S. and Yurimoto H. (2003) Relationship among O, Mg isotopes and the
702 petrography of two spinel-bearing compound chondrules. *Geochimica et Comochimica*
703 *Acta* **67**, 3943–3957.

704 Maruyama S., Yurimoto H. and Sueno S. (1999) Oxygen isotope evidence regarding the
705 formation of spinel-bearing chondrules. *Earth and Planetary Science Letters* **169**, 165–
706 171.

707 Misawa K. and Nakamura N. (1988) Highly fractionated rare-earth elements in
708 ferromagnesian chondrules from the Felix (CO3) meteorite. *Nature* **334**, 47–50.

709 Nagashima K., Krot A. N. and Huss G. R. (2012) Oxygen-isotope compositions of chondrules
710 and matrix grains in the LEW 87232, Kakangari-like chondrite. 43rd Lunar and Planetary
711 Science Conference. Abstract #1768.

712 Onuma N., Higuchi H., Wakita H. and Nagasawa H. (1968) Trace element partition between
713 2 pyroxenes and host lava. *Earth and Planetary Science Letters* **5**, 47–51.

714 Palme H., Wlotzka F., Nagel K. and El Goresy A. (1982) An ultra-refractory inclusion from
715 the Ornans carbonaceous chondrite. *Earth and Planetary Science Letters* **61**, 1–12.

716 Rubin A. E. (2004) Aluminum low-Ca pyroxene in a Ca-Al-rich chondrule from the
717 Semarkona meteorite. *American Mineralogist* **89**, 867–872.

718 Rudraswami N. G., Ushikubo T., Nakashima D. and Kita N. T. (2011) Oxygen isotope
719 systematics of chondrules in the Allende CV3 chondrite: High precision ion microprobe
720 studies. *Geochimica et Cosmochimica Acta* **75**, 7596–7611.

721 Russell S. S., MacPherson G. J., Leshin L. A. and McKeegan K. D. (2000) ^{16}O enrichments in
722 aluminum-rich chondrules from ordinary chondrites. *Earth and Planetary Science*
723 *Letters* **184**, 57–74.

724 Russell S. S., Krot A. N., Huss G. R., Keil K., Itoh S., Yurimoto H. and MacPherson G. J.
725 (2005) The genetic relationship between refractory inclusions and chondrules. In
726 *Chondrites and the Protoplanetary Disk* (eds. A. N. Krot, E. R. D. Scott, and B.
727 Reipurth). ASP Conference Series, vol. 341. Pp. 317–350.

728 Ryerson F. J., Durham W. B., Cherniak D.J. and Lanford W.A. (1989) Oxygen diffusion in
729 olivine: Effect of oxygen fugacity and implications for creep. *Journal of Geophysical*
730 *Research* **94**, 4105–4118.

731 Ryerson F. J. and McKeegan K. D. (1994) Determination of oxygen self-diffusion in
732 akermanite, anorthite, diopside, and spinel: Implications for oxygen isotopic anomalies
733 and the thermal histories of Ca-Al-rich inclusions. *Geochimica et Cosmochimica Acta* **58**,
734 3713–3734.

735 Sheng Y. J. (1992) Origin of plagioclase-olivine inclusions. Ph.D. thesis, California Institute
736 of Technology, Pasadena, California, USA. Pp 271.

737 Sheng Y. J., Hutcheon I. D. and Wasserburg G. J. (1991) Origin of plagioclase-olivine
738 inclusions in carbonaceous chondrites. *Geochimica et Cosmochimica Acta* **55**, 581–599.

739 Tenner T. J., Ushikubo T., Kurahashi E., Kita N. T. and Nagahara H. (2013) Oxygen isotope
740 systematics of chondrule phenocrysts from the CO3.0 chondrite Yamato 81020: evidence
741 for two distinct oxygen isotope reservoirs. *Geochim. Cosmochim. Acta* **102**, 226–245.

742 Tronche E. J., Hewins R. H. and MacPherson G. J. (2007) Formation conditions of
743 aluminum-rich chondrules. *Geochimica et Cosmochimica Acta* **71**, 3361–3381.

744 Ushikubo T., Kimura M., Kita N. T. and Valley J. W. (2012) Primordial oxygen isotope
745 reservoirs of the solar nebula recorded in chondrules in Acfer 094 carbonaceous
746 chondrite. *Geochimica et Cosmochimica Acta* **90**, 242–264.

747 Wakaki S., Itoh S., Tanaka T. and Yurimoto H. (2013) Petrology, trace element abundances
748 and oxygen isotopic compositions of a compound CAI-chondrule object from Allende.
749 *Geochimica et Cosmochimica Acta* **102**, 261–279.

750 Wang W. Y. and Yurimoto H. (1993) Analysis of rare earth elements in garnet by SIMS. *Ann.*
751 *Rep. Inst. Geosci., Univ. Tsukuba* **19**, 87–91.

752 Wasson J. T., Yurimoto H. and Russell S. S. (2001) ^{16}O-rich melilite in CO3.0 chondrites:
753 Possible formation of common, ^{16}O-poor melilite by aqueous alteration. *Geochimica et*
754 *Cosmochimica Acta* **65**, 4539–4549.

755 Yasuda M., Kitamura M. and Morimoto N. (1983) Electron microscopy of clinoenstatite from
756 boninite and a chondrite. *Physics and Chemistry of Minerals* **9**, 192–196.

757 Yu Y., Hewins R. H., Clayton R. N. and Mayeda T. K. (1995) Experimental study of high
758 temperature oxygen isotope exchange during chondrule formation. *Geochimica et*
759 *Cosmochimica Acta* **59**, 2095–2104.

760 Yurimoto H. and Wasson J. T. (2002) Extremely rapid cooling of a carbonaceous-chondrite
761 chondrule containing very ^{16}O-rich olivine and a ^{26}Mg-excess. *Geochimica et*
762 *Cosmochimica Acta* **66**, 4355–4363.

763 Yurimoto H., Krot A. N., Choi B.-G., Aleon J., Kunihiro T. and Brearley A.J. (2008) Oxygen
764 isotopes of chondritic components. *Reviews in Mineralogy & Geochemistry* **68**, 141–186.

765 Yurimoto H., Nagasawa H., Mori Y. and Matsubaya O. (1994) Microdistribution of oxygen
766 isotopes in a refractory inclusion from the Allende meteorite. *Earth and Planetary*
767 *Science Letters* **128**, 47–53.

768 Yurimoto H., Yamashita A., Nishida N. and Sueno S. (1989) Quantitative SIMS analysis of
769 GSJ rock reference samples. *Geochemical Journal* **23**, 215–236.

770 Zhang A. C. and Hsu W. B. (2009) Refractory inclusions and aluminum-rich chondrules in
771 Sayh Al Uhaymir 290 CH chondrite: Petrography and Mineralogy. *Meteoritics &*
772 *Planetary Science* **44**, 787–804.

773 Zhang A. C., Itoh S., Yurimoto H., Sun Q. and Wang R. C. (2011) Formation of the
774 Sapphirine-bearing Al-rich Chondrule in the DaG 978 Carbonaceous Chondrite:
775 Preliminary Mineralogical and Oxygen Isotopic Results. Workshop for formation of the
776 First Solids in the Solar System, abstract #9028.

777 Zhang A. C. and Yurimoto H. (2013) Petrography and mineralogy of the ungrouped type 3
778 carbonaceous chondrite Dar al Gani 978. *Meteoritics & Planetary Science* **48**, 1651–
779 1677.

780 Zhang A. C., Itoh S, Sakamoto N, Wang R. C. and Yurimoto H. (2013) Heterogeneous
781 oxygen isotopic compositions in a sapphirine-bearing Al-rich chondrule from the DaG
782 978 carbonaceous chondrite. 44th Lunar and Planetary Science Conference, abstract
783 #1449.

784

Figure Captions

Figure 1. Back-scattered electron (BSE) image of the sapphirine-bearing Al-rich chondrule in DaG 978. The dashed and solid lines indicate the core-mantle and mantle-rim boundaries, respectively.

Figure 2. BSE images of the core in the SARC. (a) Small spinel grains are included in anorthite, Al-rich enstatite, and sapphirine. (b) Euhedral sapphirine grains are randomly distributed in mesostasis.

Figure 3. BSE images of the mantle in the SARC. (a) Typical area in the mantle, which contains euhedral anorthite, enstatite, and mesostasis. (b) Transition zone between the core and mantle, distinguished by the presence or lack of spinel, respectively. (c) Augite grain in mesostasis up to 20 μm in size and the Fe-rich, low-Al enstatite in mesostasis is approximately 5 μm thick. (d) Several anhedral olivine grains and FeNi metal in the mantle.

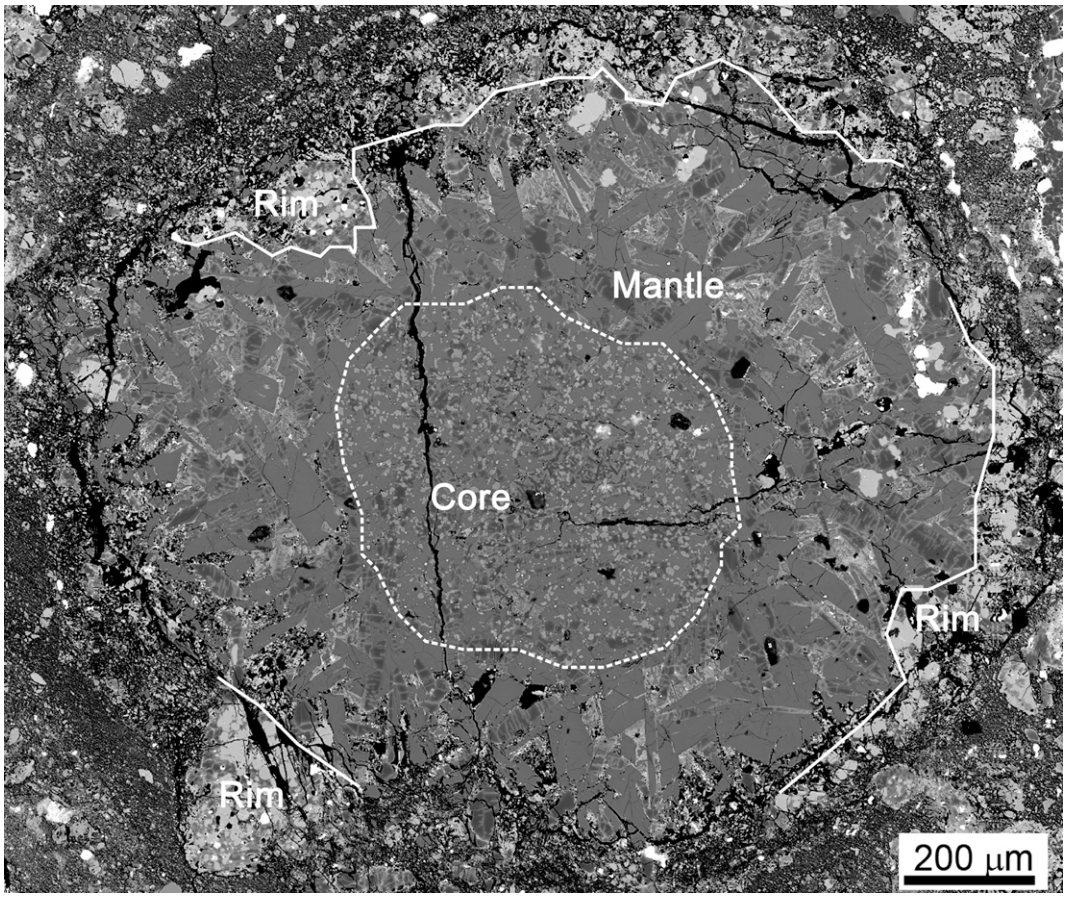
Figure 4. BSE images of the SARC rim, which mainly contains of Fe-rich olivine, enstatite, and FeNi metal. Al-en: Al-rich enstatite; an: anorthite; meso: mesostasis; sp: spinel; spr: sapphirine; en: enstatite; ol: olivine.

Figure 5. Oxygen isotopic compositions of minerals and mesostasis presented on oxygen three-isotope diagrams. Error bars denote two standard deviation (2σ). En: enstatite; an: anorthite; meso: mesostasis; sp: spinel; spr: sapphirine; ol: olivine.

Figure 6. REE pattern of mesostasis in the SARC from DaG 978. Error bars denote one standard deviation (1σ).

Figure 7. Curves showing diffusion time as a function of temperature for various diffusion lengths. Solid curves represent minimum temperatures and diffusion times for the estimated oxygen and Fe-Mg diffusion lengths observed in this study. Dashed lines represent the upper limits of temperature and diffusion time, based on estimated upper limits of O diffusion lengths in olivine and spinel. (a) Under anhydrous conditions. The diffusion coefficients for oxygen in spinel, anorthite, forsterite, and diopside under anhydrous conditions are from Ryerson and McKeegan (1994), Elphick et al. (1988), and Hallwig et al. (1982). The diffusion coefficients for Fe-Mg in spinel, forsterite, Al-poor enstatite, and diopside under anhydrous conditions are from Freer and O'Reilly (1980), Ganguly and Tazzoli (1994), Dimanov and Wiedenbeck (2006), and Chakraborty (2010). (b) Under hydrous conditions. The diffusion coefficients for oxygen in anorthite, forsterite, and diopside under hydrous conditions are from Giletti et al. (1978), Jaoul et al. (1983), and Farver (1989).

817 Figure 8. Schematic diagram for the formation of SARC in DaG 978. Diamond and rectangle
818 symbols represent spinel and olivine, respectively.
819



820

821 Figure 1.

822

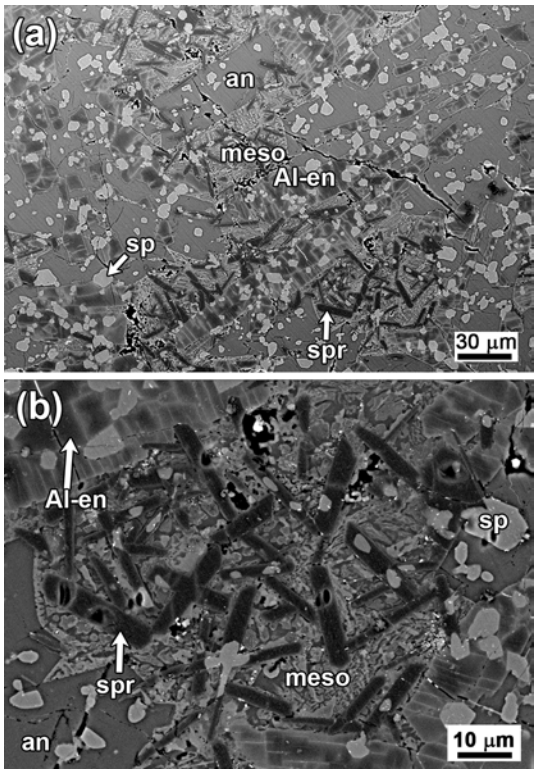
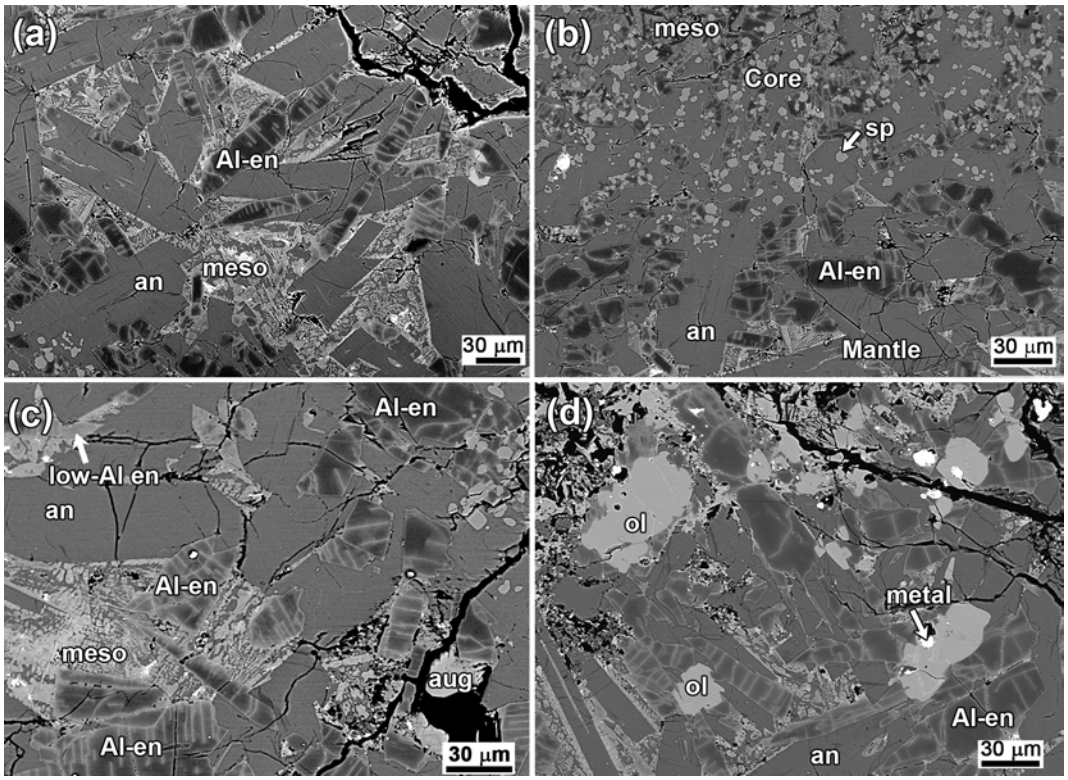


Figure 2.



826

827 Figure 3

828

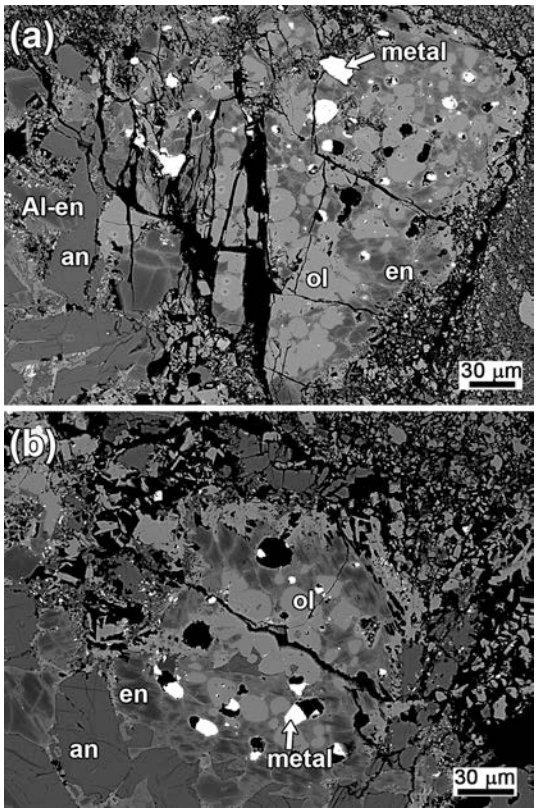
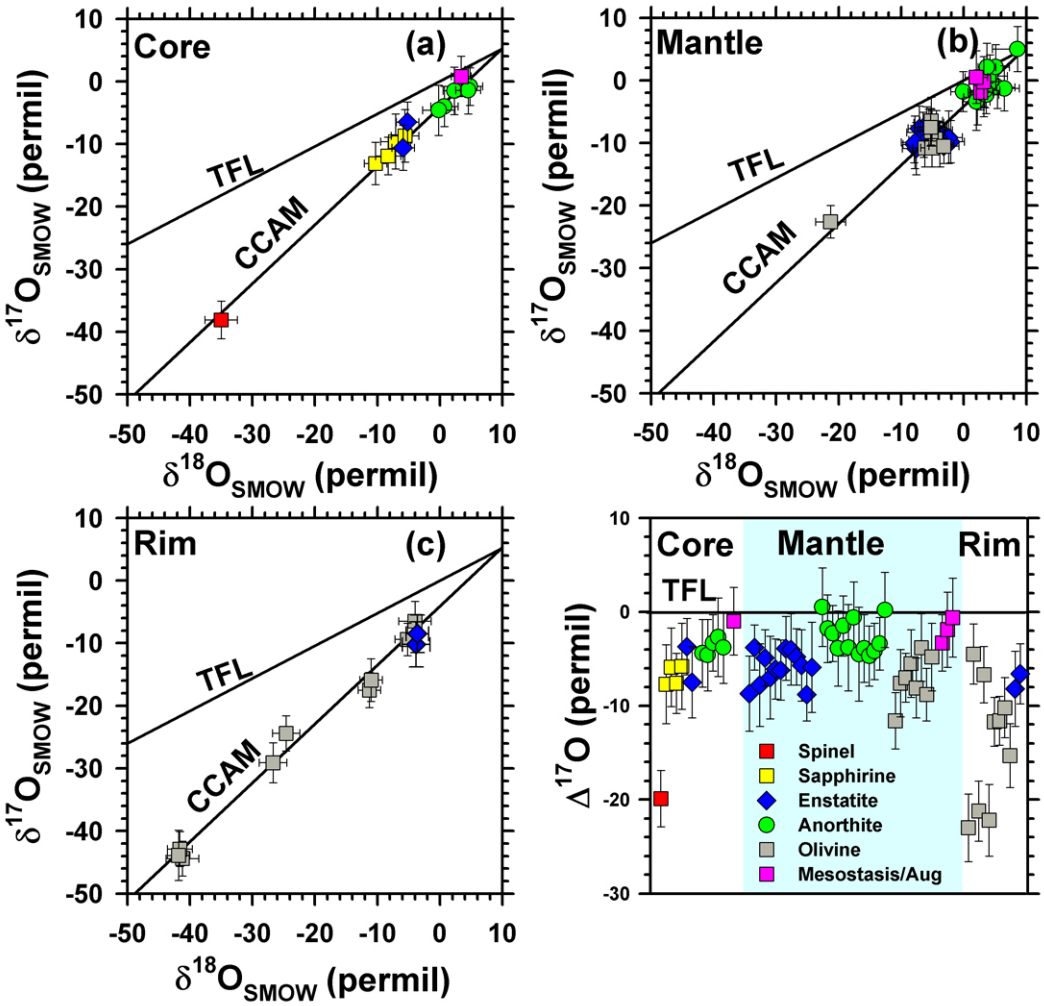


Figure 4

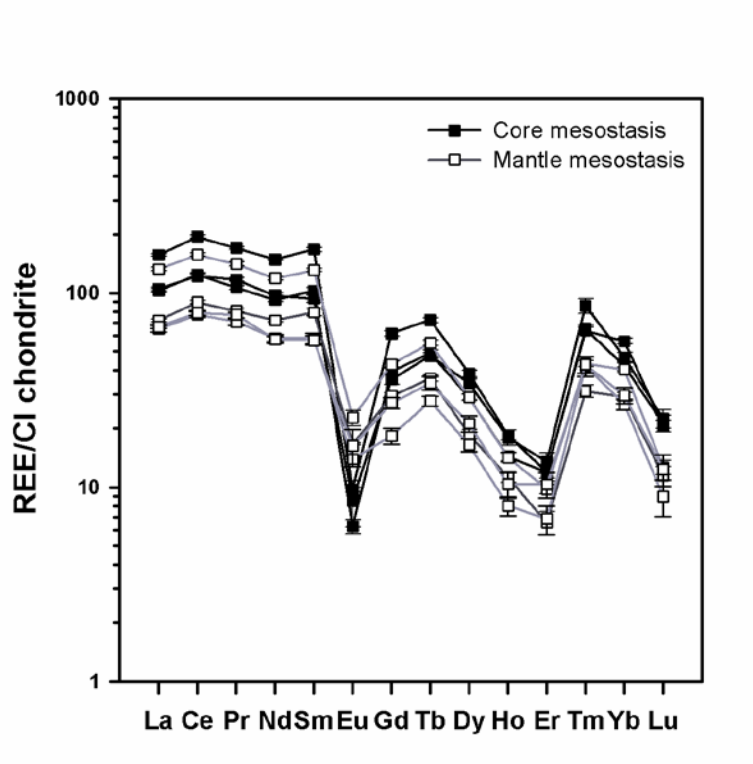


833

834 Figure 5.

835

836

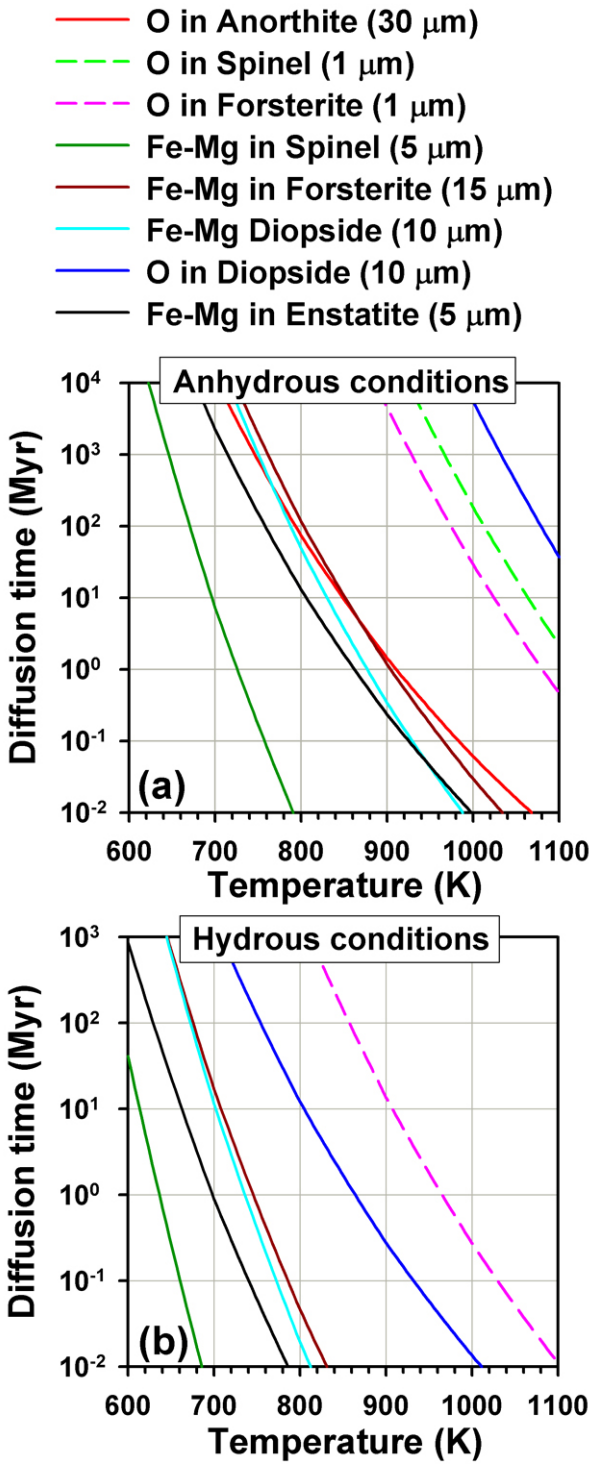


837

838 Figure 6.

839

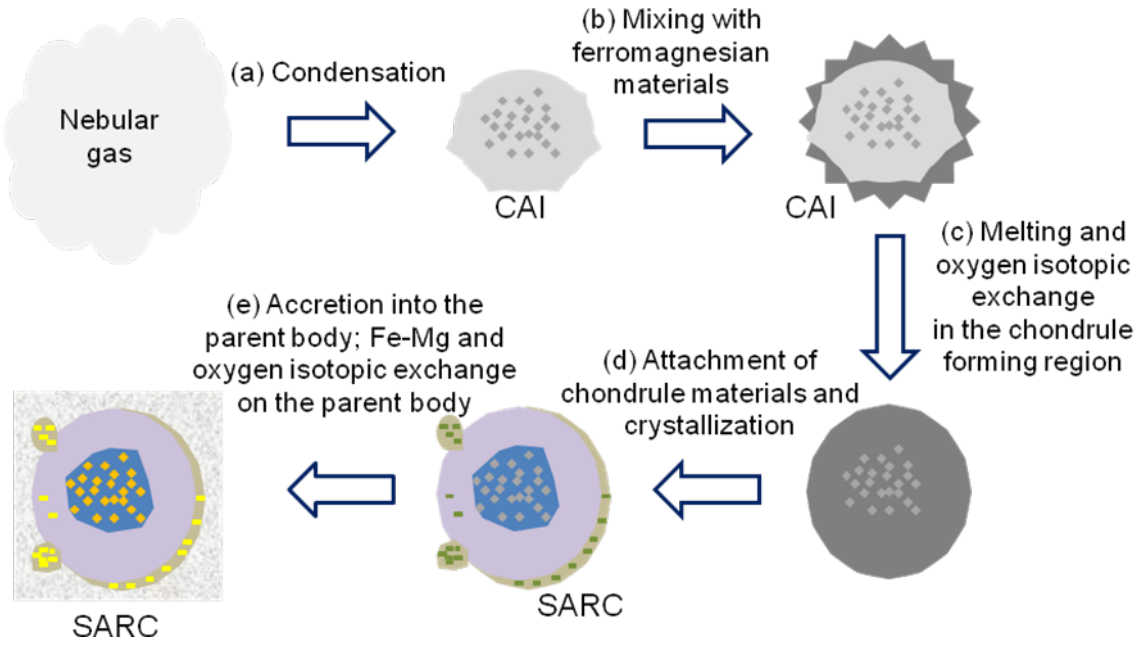
840



841

842 Figure 7.

843



844

845 Figure 8.

846

847

Table 1. Representative chemical compositions (wt%) of minerals in SARC from DaG 978

	Core minerals				Mantle minerals							Rim minerals	
	sp	spr	an	en	an	an	en	en	en	ol	aug	ol	en
SiO_2	0.14	17.9	45.9	51.1	45.0	46.9	51.2	52.0	54.3	38.2	50.9	36.9	56.0
TiO_2	0.34	1.44	0.06	1.57	0.04	0.06	1.57	1.07	1.63	0.06	0.14	0.08	0.18
Al_2O_3	65.1	54.9	34.9	10.9	35.1	33.5	10.5	3.71	4.91	bd	0.43	0.02	1.08
Cr_2O_3	1.34	1.09	bd	0.25	0.03	bd	0.34	0.28	0.47	bd	0.05	bd	0.16
MgO	14.6	23.7	bd	34.6	bd	0.18	32.8	28.4	37.3	34.9	11.2	34.4	36.8
MnO	0.12	0.08	0.02	0.07	bd	bd	0.11	0.26	0.24	0.28	0.11	0.39	0.07
FeO	18.0	0.40	0.21	0.37	0.23	0.31	0.37	14.0	0.73	25.8	11.3	27.7	4.64
CaO	0.10	0.16	18.1	0.68	18.1	17.2	0.74	0.74	0.69	0.05	25.1	bd	0.52
Na_2O	bd	bd	1.55	0.02	1.54	2.13	bd	0.04	0.03	bd	0.12	bd	bd
Total	99.7	99.7	100.8	99.6	100.0	100.2	97.5	100.5	100.3	99.3	99.4	99.5	99.4
					Calculated based on 24 oxygen atoms								
Si	0.022	2.494	6.311	6.925	6.239	6.468	7.059	7.437	7.330	6.086	7.823	5.945	7.722
Ti	0.040	0.150	0.006	0.160	0.004	0.006	0.162	0.115	0.165	0.007	0.016	0.010	0.019
Al	11.907	8.999	5.645	1.738	5.725	5.435	1.703	0.624	0.780	bd	0.078	0.004	0.175
Cr	0.164	0.120	bd	0.027	0.003	bd	0.037	0.032	0.050	bd	0.006	bd	0.017
Mg	3.405	4.953	bd	7.033	bd	0.037	6.783	6.093	7.552	8.341	2.582	8.313	7.612
Mn	0.016	0.009	0.002	0.008	bd	bd	0.013	0.031	0.027	0.038	0.014	0.053	0.008
Fe	2.332	0.046	0.024	0.042	0.027	0.036	0.043	1.669	0.082	3.426	1.447	3.719	0.533
Ca	0.017	0.024	2.666	0.099	2.689	2.541	0.109	0.113	0.100	0.009	4.133	bd	0.077
Na	bd	bd	0.412	0.005	0.413	0.569	bd	0.011	0.008	bd	0.036	bd	bd

Bd: below detection limit. Sp: spinel; spr: sapphirine; an: anorthite; en: enstatite; ol: olivine; aug: augite.

854 Table 2. SEM-EDS bulk compositions (wt%) of the core and mantle and their respective
855 mesostasis in SARC

	Core		Mantle	
	Bulk	Mesostasis	Bulk	Mesostasis
Na_2O	1.1	1.1	1.8	1.7
MgO	13.0	14.2	10.6	6.4
Al_2O_3	29.3	27.2	21.6	14.6
SiO_2	40.8	40.9	48.8	53.0
CaO	8.8	8.9	11.5	16.3
TiO_2	0.9	1.6	0.9	1.3
Cr_2O_3	0.9	1.4	0.3	0.1
FeO	5.4	4.6	4.5	6.6
Total	100	100	100	100

856

857

858 Table 3. Oxygen isotopic compositions (permil) of minerals and mesostasis in SARC

	$\delta^{18}O_{SMOW}$	2σ	$\delta^{17}O_{SMOW}$	2σ	$\Delta^{17}O$	2σ
Core minerals and mesostasis						
Spinel						
dag@70	-35.0	2.6	-38.1	3.0	-19.9	3.0
Sapphirine						
dag@71	-7.1	2.4	-9.6	4.4	-5.9	4.2
dag@74	-10.3	1.8	-13.1	3.4	-7.7	4.2
dag@115	-8.3	2.0	-11.9	3.0	-7.6	3.2
dag@116	-5.6	2.2	-8.7	4.2	-5.8	4.6
Enstatite						
dag@113	-5.2	1.8	-6.5	3.2	-3.7	3.0
dag@120	-5.9	1.8	-10.6	3.6	-7.5	3.8
Anorthite						
dag@107	-0.7	2.0	-3.4	3.8	-3.1	3.8
dag@108	0.7	2.2	-4.0	3.2	-4.4	3.6
dag@110	-0.2	2.6	-4.6	4.0	-4.6	3.8
dag@111	4.8	2.0	-0.8	3.0	-3.3	3.0
dag@112	2.3	1.8	-1.5	3.8	-2.7	4.2
dag@118	4.5	2.0	-1.4	3.8	-3.8	3.8
Mesostasis						
dag@122	-2.9	1.6	-5.7	4.6	-4.2	4.8
dag@125	3.4	1.6	0.8	3.2	-1.0	3.6

859

860

861 Table 3. continued

	$\delta^{18}O_{SMOW}$	2σ	$\delta^{17}O_{SMOW}$	2σ	$\Delta^{17}O$	2σ
Mantle minerals and mesostasis						
Enstatite						
dag@35	-2.1	2.2	-9.8	3.4	-8.7	4.0
dag@36	-5.6	2.4	-6.8	2.2	-3.8	2.4
dag@38	-2.4	2.2	-9.1	4.2	-7.8	4.4
dag@42	-6.5	2.6	-8.3	3.2	-4.9	3.0
dag@50	-7.6	2.2	-10.9	4.2	-7.0	4.4
dag@52	-7.9	1.8	-10.2	3.0	-6.1	3.2
dag@55	-6.4	2.4	-9.5	2.8	-6.2	3.2
dag@90	-5.9	2.0	-7.0	2.8	-3.9	3.4
dag@91	-7.1	1.8	-7.7	3.6	-4.0	3.8
dag@93	-5.1	2.2	-7.4	2.6	-4.8	3.0
dag@99	-4.4	2.6	-8.0	3.2	-5.7	3.8
dag@142	-3.2	2.4	-10.5	2.8	-8.8	2.8
dag@143	-7.8	2.2	-9.9	4.2	-5.9	4.8
Anorthite						
dag@33	4.4	2.6	-1.1	4.8	-3.4	5.0
dag@34	8.6	4.0	5.0	3.6	0.5	4.2
dag@40	-0.1	2.0	-1.8	3.2	-1.8	3.6
dag@41	3.6	1.8	-0.4	3.0	-2.3	3.0
Anorthite#1						
dag@87#1	5.4	2.8	-1.1	3.4	-3.9	4.0
dag@88#1	4.2	2.8	0.7	3.4	-1.5	3.2
dag@89	2.2	2.2	-2.7	4.4	-3.8	4.6
dag@92	5.1	2.2	2.1	3.6	-0.6	3.8
dag@94	2.0	2.2	-3.4	4.6	-4.5	5.0
dag@97	3.2	2.2	-2.2	3.6	-3.9	3.6
dag@98	6.5	2.4	-1.3	3.6	-4.7	3.2
dag@119	3.6	2.0	-2.3	3.0	-4.2	3.0
dag@138	3.4	2.4	-1.6	2.8	-3.4	2.8
dag@139	3.7	1.4	2.1	3.8	0.2	4.0
Olivine						
dag@45	-7.5	2.2	-12.3	3.4	-8.5	3.6
Olivine#1						
dag@46	-21.3	2.4	-22.6	2.6	-11.6	3.0
dag@49	-5.2	2.2	-8.2	3.6	-5.5	3.6
dag@51	-5.1	1.8	-10.8	3.0	-8.1	3.2
dag@47	-6.2	2.0	-10.8	3.0	-7.6	3.6
dag@48	-4.5	1.8	-9.4	2.4	-7.0	2.6
dag@140	-5.2	1.8	-6.5	3.8	-3.8	3.6
dag@141	-3.2	2.4	-10.5	2.8	-8.8	2.8
dag@144	-5.3	2.6	-7.5	3.0	-4.8	3.6
Mesostasis						
dag@95(aug)	5.2	2.8	-0.3	3.4	-2.9	3.6
dag@104	2.7	2.0	-1.9	2.8	-3.3	3.0
dag@105	3.2	2.4	-0.2	4.0	-1.9	4.0
dag@106	2.0	1.8	0.5	4.2	-0.6	4.2

862

863 Table 3. continued

	$\delta^{18}O_{SMOW}$	2σ	$\delta^{17}O_{SMOW}$	2σ	$\Delta^{17}O$	2σ
Rim minerals						
Olivine						
dag@56	-11.4	1.8	-14.7	3.0	-8.8	3.0
Olivine#2						
dag@57	-41.2	2.6	-44.4	2.8	-23.0	3.6
dag@62	-41.6	2.0	-42.9	2.8	-21.2	3.2
dag@131	-41.8	1.8	-43.9	4.0	-22.2	3.8
dag@59	-4.0	2.6	-6.5	3.2	-4.5	3.2
dag@129	-5.2	2.0	-9.4	2.6	-6.7	3.0
Olivine#3						
dag@132	-11.3	1.8	-17.5	2.8	-11.7	2.6
dag@133	-24.6	2.2	-24.4	2.8	-11.6	2.6
dag@135	-26.7	2.2	-29.1	3.2	-15.3	3.4
dag@134	-11.0	1.8	-15.9	3.4	-10.2	3.2
Enstatite						
dag@130	-3.8	2.2	-10.2	3.6	-8.2	4.0
dag@136	-3.6	1.8	-8.5	3.0	-6.6	3.2

864 Individual measurements are from different grains except anorthite grain#1 and olivine grains #1, #2,
865 and #3. Intra-grain heterogeneities are observed in olivine grains #1 and #3.
866

867 Table 4. REE concentrations (ppm) in the core and mantle mesostasis of SARC

	Core mesostasis								Mantle mesostasis							
	c-1	1σ	c-2	1σ	c-3	1σ	c-4	1σ	m-1	1σ	m-2	1σ	m-3	1σ	m-4	1σ
La	24.6	0.6	24.0	0.5	36.8	0.7	24.1	0.6	15.4	0.6	15.7	0.4	16.9	0.3	31.1	0.6
Ce	73.8	1.6	70.9	0.9	117.2	1.9	74.7	1.8	46.7	1.5	47.6	1.5	54.0	1.0	94.9	2.0
Pr	10.4	0.2	10.4	0.3	15.2	0.3	9.5	0.2	6.3	0.2	6.9	0.2	7.2	0.2	12.6	0.3
Nd	43.9	1.3	40.8	0.9	67.4	1.1	41.7	1.0	26.4	1.2	26.0	1.0	32.7	0.6	53.8	1.2
Sm	13.7	0.6	12.5	0.4	24.6	0.6	15.0	0.6	8.6	0.5	8.4	0.5	11.7	0.5	19.3	0.4
Eu	0.5	0.1	0.9	0.3	0.5	0.1	0.4	0.1	0.8	0.0	0.9	0.2	0.9	0.1	1.3	0.1
Gd	7.1	0.4	7.7	0.5	12.1	0.4	7.7	0.3	3.6	0.3	5.3	0.3	5.8	0.2	8.4	0.3
Tb	1.7	0.1	1.7	0.1	2.6	0.1	1.8	0.1	1.0	0.1	1.2	0.1	1.3	0.0	2.0	0.1
Dy	8.3	0.4	6.6	0.5	9.3	0.4	7.0	0.3	4.0	0.3	5.2	0.5	4.5	0.3	7.1	0.2
Ho	1.0	0.1	0.8	0.1	1.0	0.1	0.8	0.0	0.4	0.1	0.6	0.1	0.6	0.0	0.8	0.0
Er	2.1	0.2	2.2	0.4	1.9	0.1	1.9	0.2	1.1	0.2	1.6	0.2	1.0	0.1	1.6	0.1
Tm	2.1	0.2	1.9	0.2	1.6	0.1	1.6	0.1	1.0	0.1	1.0	0.1	0.8	0.1	1.0	0.0
Yb	7.5	0.5	7.0	0.4	9.2	0.3	6.8	0.4	4.3	0.3	4.8	0.5	4.7	0.3	6.5	0.2
Lu	0.5	0.1	0.4	0.1	0.5	0.1	0.5	0.1	0.2	0.0	0.3	0.1	0.3	0.1	0.3	0.1

868